Plasmonics
https://doi.org/10.1007/s11468-023-02110-6

RESEARCH

Simulation of a Sensitive Mid-infrared (MIR) D-Shaped Optical Fiber Water Pollutant Sensor

B. M. Younis[1,2] · Nada Yazeed M. Dawood[1,2] · Ahmed El-Sayed Abd-Elkader[1,3] · David Furniss[4] · Mark Farries[4] · Sendy Phang[4] · Trevor M. Benson[4] · Angela B. Seddon[4] · Mohamed Farhat O. Hameed[5,6,7] · S. S. A. Obayya[1,8]

Received: 2 October 2023 / Accepted: 23 October 2023

Abstract

In this work, an efficient optical sensor is proposed for the sensitive detection of various pollutants in water. The suggested optical sensor is based on an indium fluoride (InF_3) glass fabricated as a D-shaped optical fiber. The polished surface of the D-shaped fiber is coated with a gold grating to induce the surface plasmon resonance (SPR). The SPR depends on the optical properties of the polluted water analyte in physical contact with the grating. The proposed optical SPR fiber sensor operates within the mid-infrared (MIR) range (3000–4500 nm) to detect any slight change in the water refractive index (RI) due to any pollutants. The full vectorial finite element method (FVFEM) is utilized to calculate the modal properties of the reported sensor. High sensor sensitivity of 17,834 nm/RIU (refractive index units) is achieved for the detection of dissolution of nitric acid (HNO_3) in water at a concentration of 14% v/v (volume/volume). Additionally, the reported sensor detects the dissolution of hydrogen peroxide (H_2O_2) in water investigated at concentrations of 15% v/v and 30% v/v, with sensitivities of 12,308 nm/RIU and 17,143 nm/RIU, respectively. Further, suspending polystyrene beads of diameter 0.1 µm in the water at a concentration of 10% v/v gives a maximum sensitivity of 5333 nm/RIU. Therefore, the proposed sensor provides a promising approach for the detection of water pollutants in the MIR wavelength regime, rather than the weaker response in the near infrared.

Keywords Refractive index sensor · Surface plasmon resonance · Water pollution · Optical fibers · Finite element method

Introduction

Owing to the huge recent development of cities in countries worldwide, water is exposed to many pollutants including chemical and biological pollutants and hazardous heavy metal ions [1–3]. Numerous pollution sources, such as waste products of industry (e.g., acetone from silicon foundries) and agriculture (nitrates, pesticides, etc.), are disposed of in rivers leading to environmental pollution. The impact of excessive pollutants in drinking water can cause human

✉ Mohamed Farhat O. Hameed
mfarahat@zewailcity.edu.eg

✉ S. S. A. Obayya
sobayya@zewailcity.edu.eg

[1] Centre for Photonics and Smart Materials, Zewail City of Science, Technology and Innovation, October Gardens, 6th of October City 12578, Egypt

[2] Electronics and Communications Engineering Department, Misr Higher Institute for Engineering and Technology (MET), Mansoura, Egypt

[3] Electronics and Communications Engineering Department, Faculty of Engineering, Delta University for Science and Technology, Gamasa, Dakahlia, Egypt

[4] Mid-Infrared Photonics Group, George Green Institute for Electromagnetics Research, Faculty of Engineering, University of Nottingham, Nottingham NG7 2RD, UK

[5] Nanotechnology and Nanoelectronics Engineering Program, Zewail City of Science, Technology and Innovation, October Gardens, 6th of October City, Giza 12588, Egypt

[6] Centre of Nanotechnology, Zewail City of Science, Technology and Innovation, October Gardens, 6th of October City 12578, Egypt

[7] Department of Mathematics and Engineering Physics, Faculty of Engineering, University of Mansoura, Mansoura 35516, Egypt

[8] Department of Electronics and Communication Engineering, Faculty of Engineering, University of Mansoura, Mansoura 35516, Egypt

Published online: 11 November 2023

morbidity and mortality, such as kidney failure, cardiovascular disease, nervous system failure, cancer, and brain damage [4, 5]. Additionally, polluted water has undesirable ecological effects on wildlife and marine life [6–9]. Therefore, the development of sensors for detecting, and monitoring, pollutants in water is a significant worldwide challenge. Among pollutant sensors, optical sensors [10] promise stability, sensitivity, a wide detection range, compactness, and short response time [11–13]. An important optical sensing mechanism is surface plasmon resonance (SPR) [14]. SPR refers to enhancement of the sensitivity of an optical sensor by a collective oscillation of free electrons, known as a surface plasmon wave, excited at a metal-dielectric interface. SPR is generated on coupling between the surface plasmon waves on a metal surface when irradiated with total internal reflection (TIR) evanescent waves from the dielectric, here a glass optical fiber, under certain conditions. When the wave vector of the fundamental fiber core mode (excited by an incident light wave) and the surface plasmon wave coincide, a distinct loss peak is obtained in the loss spectrum of the fundamental core mode. The resonance condition is satisfied at a particular wavelength known as the resonance wavelength, which is highly sensitive to the nature of the dielectric medium surrounding the metal film. Thus, if the optical properties of the dielectric medium should change, then the effective refractive index of the surface plasmon mode also changes. Accordingly, the resonance wavelength corresponding to the loss peak shifts its position towards longer or shorter wavelengths when analyte molecules bind over the plasmonic layer. Hence, the SPR optical sensing technique is sensitive to the presence of the analyte molecule through the change in RI. Such sensors offer potential for medical, biological, and chemical sensing, and for environmental monitoring [15–17].

Prisms and optical fibers are platforms to excite SPR because of their TIR phenomenon; but prisms are bulky [18] and fiber offers the more compact, possibly more economical, platform [19] as well as a remote sensing opportunity [20]. As the plasmonic optical fiber sensors depend on phase matching between the fiber core-guided mode and the surface plasmon polaritons (SPPs) [21], a convenient design format is the D-shaped (side-polished, then metal coated) optical fiber-based SPR sensor. Here, the incident light travelling in the fiber is coupled out into the thin metallic film [22]. Kadhim et al. [23] in 2020 proposed and simulated a SPR D-shaped, silica-glass, single-mode optical fiber sensor with silver grating; the D-shape exposed the fiber core. The sensor operated in the visible wavelength regime and when the RI of the theoretical analyte was varied between 1.33 and 1.39, the sensor showed RI sensitivity of 6400 nm / RIU [23]. Verma et al. [24] fabricated a silica-glass, single-mode optical fiber SPR sensor. The active surface was composed of a multi-layer of pyrrole/chitosan/ITO/Ag coated onto an optically unclad area of the fiber. Heavy metal ions, Cd^{2+}, Pb^{2+}, and Hg^{2+}, were detected in contaminated water in the visible regime. The sensor detection limit for Cd^{2+} was 0.8 ppb and maximum sensitivity 0.418 nm per µg/l, up to a maximum of 70 µg/l beyond which the sensitivity became zero. Further, Villar et al. [25] simulated numerical NIR spectra and collected experimental NIR spectra with a D-shaped coated, single-mode, silica-glass fiber. Two different nano-coatings were analyzed: (i) a high RI continuous coating, 92 nm thick of indium tin oxide (ITO), and (ii) a layer-pair of poly(allylamine hydrochloride) (PAH) and poly(acrylic acid) (PAA), with 63 repeat layer-pairs deposited to achieve the desired thickness. Both operated in the NIR regime. The maximum sensitivity and figure of merit were 1566 nm/RIU and 1021/RIU, respectively, within a RI variation between 1.3 and 1.335. Pathak et al. [26] presented a SPR nominally D-shaped single-mode, silica-glass, optical fiber sensor with the concave hole above the exposed fiber core. The sensor was simulated for two types of sensing structures: coated with (i) gold (Au) film or (ii) Au nanowires, respectively. The 0.4 µm diameter, round-cross-section Au wires were designed, aligned, and touching along their length inside a concave "hole" in the fiber. The theoretical sensitivity reached 4471 nm/RIU using the Au nanowires, which compared favorably to a sensitivity of only 809 nm/RIU using the continuous Au coating, for RI, 1.33 to 1.38. Additionally, Dubey et al. [27] proposed two D-shaped optical fiber-based sensors in the NIR regime. The first design had Ag grating coated with titanium dioxide (TiO_2), while the other had a tin dioxide (SnO_2) layer on the core-cladding interface, with sensitivities of 15310 nm/RIU and 9810 nm/RIU, respectively [27].

All the aforementioned sensors [23–27] were designed to operate in the visible or NIR wavelength regimes. Yet, the fundamental vibrational absorption of, for instance, organic pollutant molecules is in the mid-infrared (MIR) regime [28], where extinction coefficients are ~10^5 times greater than those in the NIR overtone and combination vibrational absorption regime. Silica glass optical fibers are transmissive in the visible regime and also in the NIR (0.7–3 µm) [29] but are opaque in the MIR regimes (3–50 µm) [29]. To circumvent this limitation of silica glass fibers, other suitable materials are required to substitute silica. Chalcogenide glasses [30] or halide glasses [31] exhibit transparency in the MIR region. As a first step, indium fluoride (InF_3)-based optical fibers were investigated here. InF_3-based optical fibers have a transmission window from the ultraviolet (UV) to 5500 nm [32] (depending on length) and are available commercially (Le Verre Fluoré) with a loss of 0.05 dB/m at 3000 nm wavelength [33].

In this work, an InF_3 glass-based D-shaped, single-mode optical fiber SPR sensor is proposed to operate in the MIR regime. The simulation addresses SPR sensing of various

pollutants in water, viz. nitric acid (HNO_3), hydrogen peroxide (H_2O_2), and polystyrene beads. A grating structure of gold (Au) nano-strips is arranged directly above the core region of the polished back D-shaped fiber to enhance the sensing performance with the *aqueous* analyte atop the Au grating.

The numerical analysis of the InF_3-based glass, D-shaped, single-mode optical fiber SPR sensor with Au grating is performed using the full vectorial finite element method (FVFEM) [34–36]. The effect on sensor performance of the Au grating thickness, width and duty cycle, and the distance from the fiber center to the underneath of the deposited Au grating are presented. A tolerance study of the potential manufacturing route is performed, including grinding and polishing to make the D-shape fiber [32]. We demonstrate the highest sensitivity for analyte detection for the simulated MIR SPR fiber sensor than ever previously demonstrated before in the visible [23, 24], NIR [25–27, 37–39], and MIR [40] regions. Additionally, the reported sensor has the advantage of a simple design. On the other hand, the proposed sensor is limited to specific pollutants with specific concentrations (14% v/v HNO_3, 15% v/v H_2O_2, 30% v/v H_2O_2, and 10% v/v polystyrene beads) in water. However, this study can be further extended to lower concentrations of the studied pollutants and/or investigating new pollutants such as heavy metals and chemical pollutants in water.

Design and Fabrication Considerations

Figure 1 depicts the proposed optical sensor setup for the simulation and the 2D cross-sectional view of the proposed SPR D-shaped InF_3-based glass, single-mode optical fiber sensor. The fiber core diameter is 50 µm and the fiber outside diameter is equal to 250 µm, making the cladding thickness, 100 µm. The proposed fiber is side-polished to a height (h) of 5 µm from the center of the fiber core, to give a large plane sensing region (Fig. 1). The RIs of the core and cladding glasses are wavelength dependent and are taken from Salem et al. [41]; at $\lambda = 3500$ nm, the core refractive index is 1.488, while cladding RI is 1.466 [41] and so the calculated fiber numerical aperture (NA) is 0.24. The Au grating thickness (t_g, correlates to thickness of Au deposited coating) is set to 50 nm; the width of each Au grating strip (w_g) and the grating period (Λ) are taken 0.4 µm and $\Lambda = w_g/\eta$, respectively, where $\eta = 0.7$ is the duty cycle defined as the ratio between the grating width and the period of Au strips.

Gold (Au) is commonly employed in SPR-based sensors due to it being chemically inert and having exceptional plasmonic properties [42]. The dielectric constant of Au is calculated via the Drude–Lorentz model in Eq. (1) [43].

$$\varepsilon_m = \varepsilon_\infty - \frac{\omega_D^2}{\omega\left(\omega - j\gamma_D\right)} - \frac{\Delta\varepsilon \cdot \Omega_L^2}{\left(\omega^2 - \Omega_L^2\right) - j\Gamma_L\omega} \tag{1}$$

where ω is the angular frequency of the guided wave, γ_D is the damping frequency, ω_D is the plasma frequency, $\varepsilon_\infty = 5.9673$ is the high frequency dielectric constant, $\Delta\varepsilon = 1.09$ is the weighted coefficient, and Γ_L and Ω_L are the bandwidth and frequency of the Lorentz oscillator. Here, $\gamma_D/2\pi = 15.92$ THz, $\omega_D/2\pi = 2113.6$ THz, $\Omega_D/2\pi = 650.07$ THz, and $\Gamma_L/2\pi = 104.86$THz.

The same setup in Goya et al. [33] can readily be applied here, where the D-shaped side-polished fiber was fabricated using standard grinding and polishing. Also, as in Goya et al. [33], the InF_3-based glass fiber was bonded in a V-grooved metal fiber holder using an UV-(ultraviolet)-curable epoxy

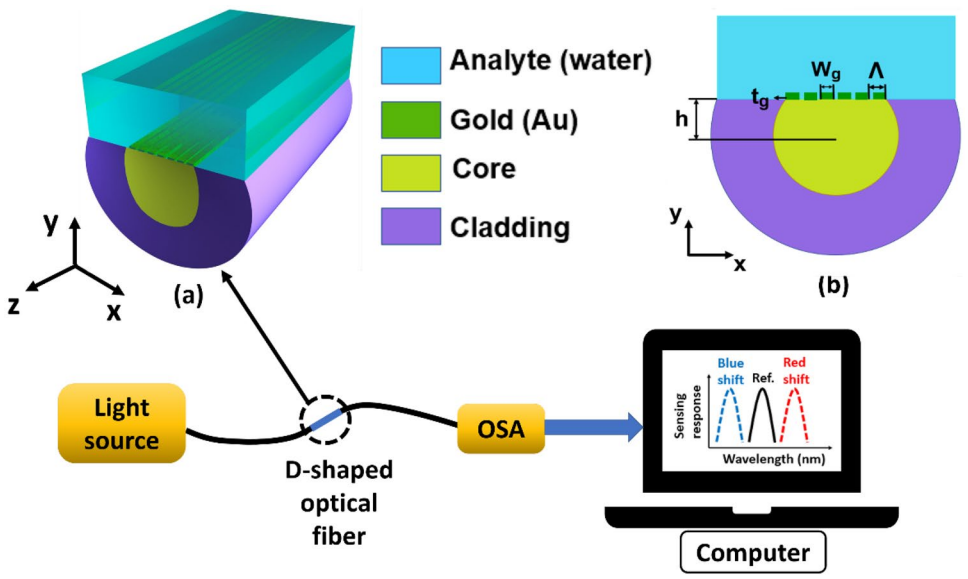

Fig. 1 Schematic of the proposed optical circuit of the simulated D-shaped InF_3-based glass, optical fiber SPM sensor setup: **a** 3-dimensional view of D-shaped fiber and **b** 2-dimensional cross section of D-shaped fiber

resin to avoid fiber fracture, as fluoride glasses exhibit a low Young's modulus and hardness compared to silica glass. To fabricate the Au grating, first, an Au layer can be deposited on the polished surface of the D-shaped InF_3-based glass fiber via thermal evaporation, magnetron sputtering, or pulsed laser deposition [23] and then the grating patterned into the deposited Au coating using nanolithography [23].

The notional sensor optical circuit (Fig. 1) comprises a commercially available (Le Verre Fluoré) delivery fiber to couple broadband light from a MIR source into the core of the D-shaped InF_3-based glass optical fiber. During the light propagation down the core of the D-shaped optical fiber, SPs are excited at the metallic/dielectric interface. Then, maximum loss is obtained at the resonance wavelength which can be detected using the optical spectrum analyzer (OSA) placed at the end of the D-shaped InF_3-based glass optical fiber and PC analyzed.

Simulation Results

Initial Studies

The modal characteristics of the proposed D-shaped fiber are analyzed via COMSOL Multiphysics software package [44] based on FVFEM. A two-dimensional FEM is set up using an electromagnetic wave frequency domain (ewfd) solver where the maximum mesh element size is 1 µm. However, the thin plasmonic strips have a small mesh element size of 2 nm to maintain the simulation accuracy. A perfectly matched layer (PML) [45] boundary condition is applied to truncate the simulation region from all transverse directions. After performing an optimization study, a PML thickness of 1 µm is used to ensure numerical stability of the obtained results. The modes supported by the suggested structure are characterized by two main parameters: mode effective index (n_{eff}) and confinement loss (L). Here, L is calculated from the imaginary part of the mode's n_{eff} as in Eq. (2) [46].

$$Confinement\ \ loss\,(L) = 8.686 \times \frac{2\pi}{\lambda(nm)} \times \left\{imag\left(n_{eff}\right)\right\} \times 10^{7} dB/cm \quad (2)$$

where λ is the wavelength and n_{eff} is the complex mode effective refractive index.

In order to prove the high accuracy of our numerical results, a comparison is performed with a D-shaped fiber that has been fabricated and simulated in [25]. Such a D-shaped fiber [25] has a solid core with a diameter of 8.2 µm, and a silica cladding region with a diameter of 125 µm. Moreover, a 92-nm coating of indium tin oxide (ITO) is deposited on the etched surface of the D-shaped fiber [25]. Figure 2 shows the measured (blue line) [25] and calculated theoretically (red line) transmissions through the D-shaped optical fiber reported in [25]. The dashed black line represents the calculated transmission based on our numerical model. It may be noted from this figure that a very good agreement between our simulated results and those reported experimentally and theoretically in [25] is obtained. This ensures the high accuracy of the reported numerical calculations.

The function of the proposed and simulated SPR-based D-shaped optical fiber sensor is to detect different pollutants in water. Nitric acid (HNO_3) is one of the water contaminants which may be dissolved in water with a concentration of 14%$^{v}/_{v}$ [47]. The proposed device can sense the polluted water by detecting the shift in the resonance wavelength due to the RI change between pure and polluted water [47, 48]. It is worth mentioning that these data are taken at a temperature of 25°C (±1°C) [2]. In addition, in the studied wavelength range, water RI changes only slightly with temperature so the temperature dependence is not considered in this study. Figure 3a, b depicts the wavelength dependent real part and imaginary part of the refractive index of pure water and those of 14% $^{v}/_{v}$ HNO_3 in water (polluted water), respectively. As may be seen in Fig. 3a, the RIs for both pure water and 14% v/v HNO_3 in water have two dips in the real parts at $\lambda = 2802$ nm (with $n = 1.14$) and at 2756 nm (with $n = 1.13$), respectively. Additionally, at $\lambda = 3150$ nm for pure water and $\lambda = 3192$ nm for 14% v/v HNO_3 in water, the RIs reach their maximum values of 1.48 and 1.44, respectively. In addition, in Fig. 3b, the maximum values of the extinction coefficients for pure water and 14% v/v HNO_3 in water occur at $\lambda = 2950$ nm (with $\kappa = 0.298$) and $\lambda = 2936$ nm (with $\kappa = 0.262$). Notably a distinct variation around $\lambda = 3000$ nm

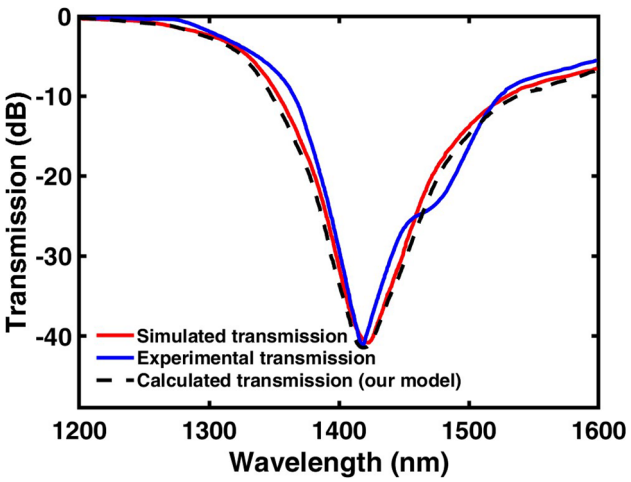

Fig. 2 The measured (blue line) [25] and calculated theoretically (red line) transmissions through D-shaped optical fiber [25] with 8.2 µm core diameter, 125 µm cladding diameter and 0.092 µm ITO thickness layer. The dashed black line represents the calculated transmission based on utilized model in our numerical simulations

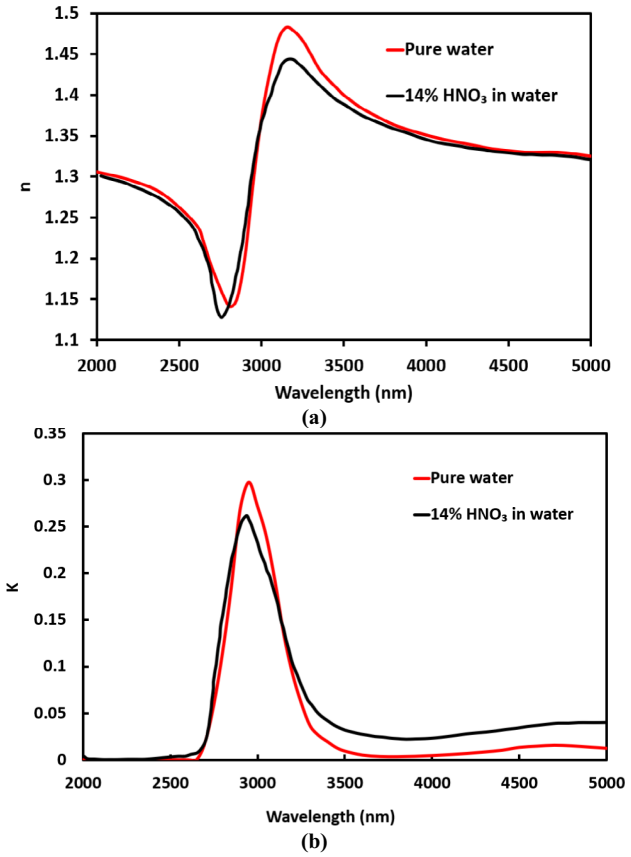

Fig. 3 **a** Real and **b** imaginary parts (*i.e.,* the extinction coefficient), of the refractive index of pure water and 14%$^{v}/_{v}$ HNO_3 polluted water due to fundamental vibrations of O–H of water at ~ 3 µm wavelength [47, 48]

is observed in both the real and imaginary parts of water RI due to the 14%$^{v}/_{v}$ addition of HNO_3 dissolved in the water. Thus, a different optical behavior is expected due to the perturbation of the water RI by the dissolved HNO_3. This behavior change is then exploited here to optimize the sensitivity of the proposed sensor.

The dispersion characteristics and optical loss spectrum of the fundamental core mode and SPM with pure water in contact with the Au grating are depicted in Fig. 4. The black curve refers to the confinement loss of the core mode, and the red (solid) and blue (dotted) curves represent the real parts of the effective refractive indices of the core mode and the SPM, respectively. From Fig. 4, the real (n_{eff}) of the core mode and the SPM both decrease with increasing wavelength. An intersection between the two effective indices of the two modes occurs at $\lambda = 3663$ nm (i.e., the resonance wavelength, λ_r) where the confinement loss of the core mode exhibits a distinct optical loss peak of about 67.8 dB/cm due to the strong coupling between the core mode and SPM. This coupling is induced thanks to the phase matching condition at which real (n_{eff}) of the fiber core mode is identical to that of the SPM. This strong coupling is confirmed by the coincidence of the optical loss peak and the intersection between the core mode and SPM effective indices.

Figure 5a, b shows the electric field distributions of the core mode at $\lambda = 3450$ nm and $\lambda = 3950$ nm away from λ_r (SPR wavelength) while Fig. 4c, d depicts the field profiles of the core mode and SPM at $\lambda_r = 3663$ nm. From Fig. 5, the coupling strength of the core mode at $\lambda_r = 3663$ nm (Fig. 4c) is higher than that at $\lambda = 3450$ nm (compared to Fig. 4a) and $\lambda = 3950$ nm (compare Fig. 4b). Additionally, at $\lambda_r = 3663$ nm, there is a strong coupling between the core mode and SPM, revealed by the strong overlap between the two modes as may be seen from Fig. 5c, d (i.e., the field profiles of these two modes are very similar as shown). It is evident from Fig. 5c, d that large power transfer will occur from the core-guided mode to the SPM due to the phase matching

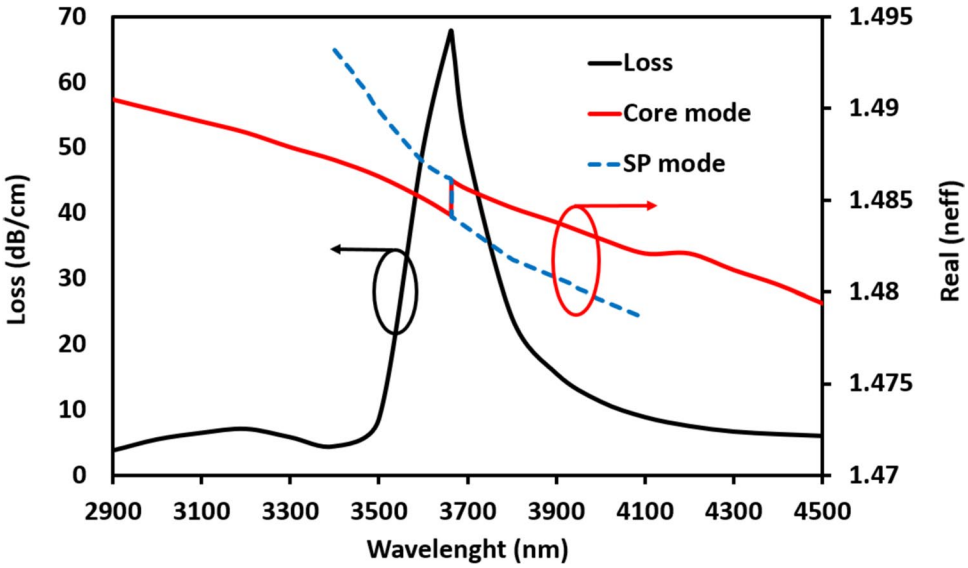

Fig. 4 Wavelength dependent confinement optical loss (black curve) and effective refractive indices of the x-polarized core mode (red curve) and SPM (blue curve) supported by the proposed D-shaped optical fiber structure, for dimensions (see Fig. 1b) of the Au grating selected to be: $t_g = 50$ nm (thickness of Au coating), $w_g = 0.4$ µm (width of patterned grating strip), $\eta = 0.7$ (duty cycle), and $h = 5$ µm (height of Au coating above the fiber core)

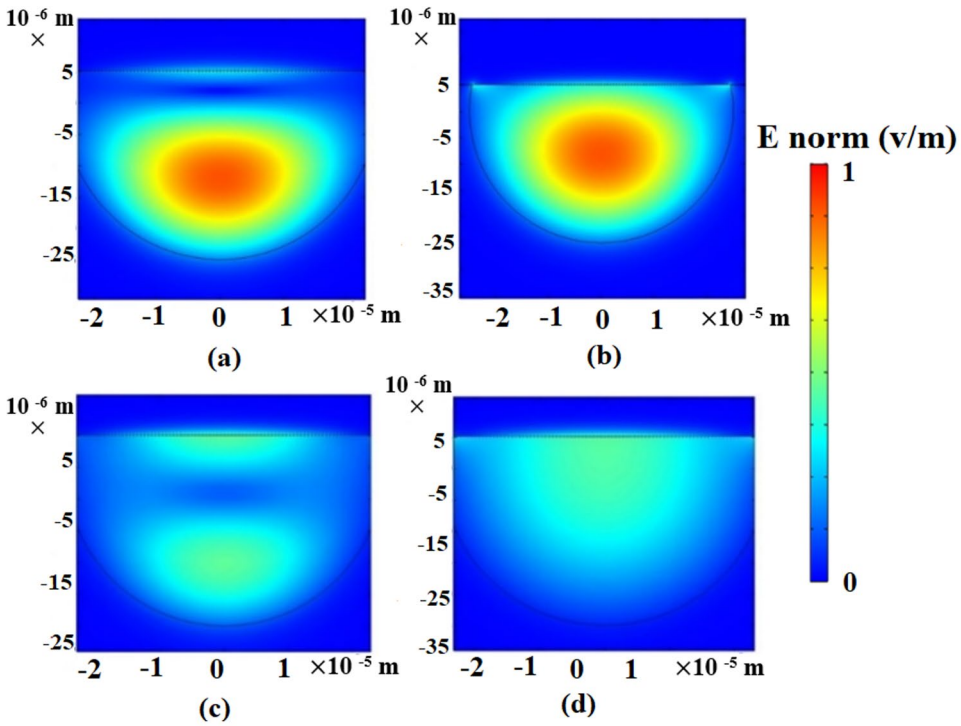

Fig. 5 E(electric)-field distribution of the: **a** core mode at $\lambda = 3450$ nm; **b** core mode at $\lambda = 3950$ nm; **c** x-polarized core mode at $\lambda_r = 3663$ nm, and **d** SPM at $\lambda_r = 3663$ nm, for Au grating dimensions of $t_g = 50$ nm, $w_g = 0.4$ µm, $\eta = 0.7$, and $h = 5$ µm (see Fig. 1b)

condition. Therefore, maximum optical loss of the core-guided mode occurs at λ_r, as revealed by the optical loss spectrum depicted in Fig. 4.

Note that only the fundamental x-polarized core mode is coupled with the SPM; in contrast, the fundamental y-polarized core mode remained well-confined in the core region with negligible coupling with the SPM. Therefore, only the fundamental x-polarized core mode is considered for all subsequent simulations.

It is well-known that the performance of SPR sensors is affected by the shift in the resonance wavelength ($\Delta\lambda_r$) for a particular change in the refractive index (Δn) of the analyte (here, the water sample). It is found here that a slight change in the RI of the water sample produces remarkable sensor sensitivity, as λ_r adapts to variations in the RI of the sensing medium, water. The SPR sensor sensitivity at a specific wavelength ($S(\lambda)$) is calculated using Eq. (3) [49]:

$$S(\lambda) = \frac{\Delta\lambda_r}{\Delta n_{ana}}(nm/RIU) \tag{3}$$

where $\Delta\lambda_r$ and Δn_{ana} are the resonance wavelength shift and the variation of the RI of the analyte, respectively. Another important parameter is the full width at half maximum (FWHM) of the optical loss curve of the fundamental x-polarized core mode. The FWHM of the optical loss curve has a direct influence on the detection accuracy (DA) which is the inverse of FWHM (Eq. (4)) [23]. Therefore, a narrow FWHM produces optimal DA [23].

$$DA = \frac{1}{FWHM} \tag{4}$$

Unfortunately, in some cases, the increase in sensitivity is accompanied by a decrease in DA leading to a trade-off between them [50]. Therefore, a figure of merit (FOM) is proposed here to help evaluate the sensor performance. We define the FOM as the ratio between the sensitivity ($S(\lambda)$, see Eq. (3)) and the FWHM as depicted in Eq. (5). So, the larger the FOM, the better the sensitivity and the detection limit [51]:

$$\text{FOM} = \frac{\text{S}}{\text{FWHM}}\text{RIU}^{-1} \tag{5}$$

When pure water is polluted with $14\%^{v}/_{v}$ nitric acid, a wavelength shift in the optical loss peak is expected to occur owing to the change in the RI of water. Figure 6 shows the wavelength-dependent confinement loss of the core mode for both pure and polluted (with $14\%^{v}/_{v}$ HNO_3) water. From Fig. 6, it may be seen that the resonance loss peak, which corresponds to the polluted water sample, is shifted to a shorter wavelength ($\lambda_r = 3560$ nm) with an increase in the confinement optical loss of the core mode. This means that a $\Delta\lambda$ of 103 nm occurs due to the change in water purity when there is a dissolution in the water of $14\%^{v}/_{v}$ HNO_3. Accordingly, the calculated sensitivity for detecting HNO_3 in water of this D-shaped InF_3-based glass optical fiber SPR optical sensor (S, Eq. (3)) is equal to 25,470 nm/RIU with DA of 11.25 μm^{-1} and FOM = 286.69 RIU^{-1}. It is worth noting

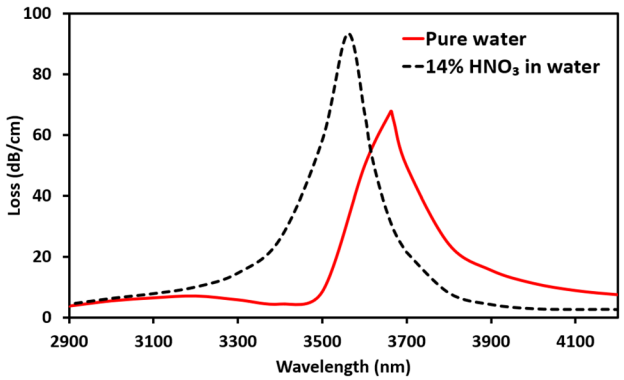

Fig. 6 Confinement optical loss spectra of the core mode for both pure water and 14% $^{v}/_{v}$ HNO_3 in water. The dimensions of the Au grating in the D-shaped InF_3-based glass optical fiber SPR optical sensor are $t_g = 50$ nm, $w_g = 0.4$ µm, $\eta = 0.7$, and $h = 5$ µm (see Fig. 1b)

that the sensor operation is limited by the available optical constants (n and k) of different concentrations of HNO_3 in water and actually applied detection to 14% $^{v}/_{v}$. So, at present, we cannot test other concentrations with our proposed sensor. However, the high sensitivity obtained here reveals the efficiency of the detection process that may be extended to at least an order of magnitude lower.

Optimizing the Sensor for Detection of 14%v/v HNO_3 Pollutant in Water

The sensor is optimized for detection of 14%$^{v}/_{v}$ HNO_3 pollutant in water. Thus, the geometrical parameters of the Au nano-grating in the proposed D-shaped InF_3-based glass fiber SPR sensor are varied one at a time, while keeping the others constant. Each geometrical parameter is tested to investigate its effect on the sensor performance indicators including sensitivity (S, Eq. (1)), detection accuracy ((DA), Eq. (4)), and figure of merit (FOM Eq. (5)) exclusively for the detection of 14%$^{v}/_{v}$ HNO_3 pollutant in water; other pollutants are addressed later in the "Projected Fabrication Tolerance of Proposed Optimized Sensor" section. The following "Au Nano-grating Thickness (tg)" to "Summary of Optimized Au Nano-grating Parameters of the Sensor" sections report varying the Au nano-grating thickness (t_g), duty cycle (η), width (w_g), and distance from the side-polished surface of the fiber to the center of the fiber core (h), respectively.

Au Nano-grating Thickness (t_g)

It is found that the surface plasmons are strongly influenced by the Au nano-grating thickness, t_g. Figure 7a shows the wavelength-dependent optical loss spectra for t_g varied from 30 to 50 nm, with a 5-nm step. By increasing t_g, λ_r is shifted to shorter wavelengths from $\lambda_r = 3710$ nm (at $t_g = 30$ nm) to 3665 nm (at $t_g = 50$ nm) for pure water and from $\lambda_r = 3610$ nm (at $t_g = 30$ nm) to 3560 nm (at $t_g = 50$ nm) for water polluted with 14% $^{v}/_{v}$ HNO_3. Additionally, the maximum values of the optical loss curves change with the variation in t_g.

From Fig. 7a, as t_g is increased from 30 to 50 nm, the confinement loss of the fundamental x-polarized core mode became *smaller* in the case of a pure water analyte. This may be explained as follows. On increasing t_g, the area of interaction between the light in the fiber core and the lossy by nature Au layer would tend to increase. Moreover, water exhibits a large extinction coefficient (κ) (Fig. 3b) at 2.7–3 µm. However, in the wavelength region from $\lambda = 3600$ to 4000 nm, the real part of the RI of pure water is quite small (< 1.4) making the RI contrast between the InF_3-based glass fiber core (1.48–1.51 for commercially available InF_3-based glass fiber) and the cladding (pure water) large. Thus, the mode is well confined in the InF_3-based glass fiber core region and there is only weak interaction between the water analyte and Au grating nano-strips, leading to small loss values of the confined mode in the fiber core.

In contrast to the pure water analyte, for water polluted with 14%$^{v}/_{v}$ HNO_3 on increasing t_g, the confinement loss is observed to *increase*; in addition, the optical loss curves became narrower. This may be explained by the now higher refractive index of the *aqueous* HNO_3 analyte (> 1.4) in the wavelength range from 3400 to 3600 nm leading to large leakage from the fundamental confined core mode through the Au nano-grating to the polluted water analyte cladding.

Figure 7b shows the sensitivity (S, Eq. (3)) and FOM (Eq. (5)) as functions of t_g for the detection of the HNO_3 pollutant. A maximum sensitivity of 28,025 nm/RIU is achieved at $t_g = 35$ nm and $t_g = 40$ nm. However, the optical loss spectra in Fig. 7a show large FWHM of 127.77 nm and 110.97 nm for $t_g = 35$ nm and $t_g = 40$ nm, respectively. A large FWHM leads to uncertain pollutant detection due to the inherent spectral noise which affects the accuracy of the detection process [47]. Therefore, the FOM is investigated (Eq. (5)). From Fig. 7b, the highest FOM observed is 286.69 RIU^{-1} at $t_g = 50$ nm, due to a small FWHM = 88.87 nm. Henceforward, t_g is therefore fixed at 50 nm in the subsequent studies to ensure accurate detection.

Au Nano-grating Duty Cycle (η)

The gold nano-grating parameters, duty cycle (η) and grating width (w_g), are next investigated to see if they could be optimized to further improve the performance of the proposed D-shaped InF_3-based glass fiber SPR sensor; η and w_g are expected to influence coupling between the D-shaped fiber core-guided mode and the SPM. The w_g investigation is reported in the "Au Nano-grating Width (wg)" section. η is first investigated and varied from 0.6 to 0.8, in steps of

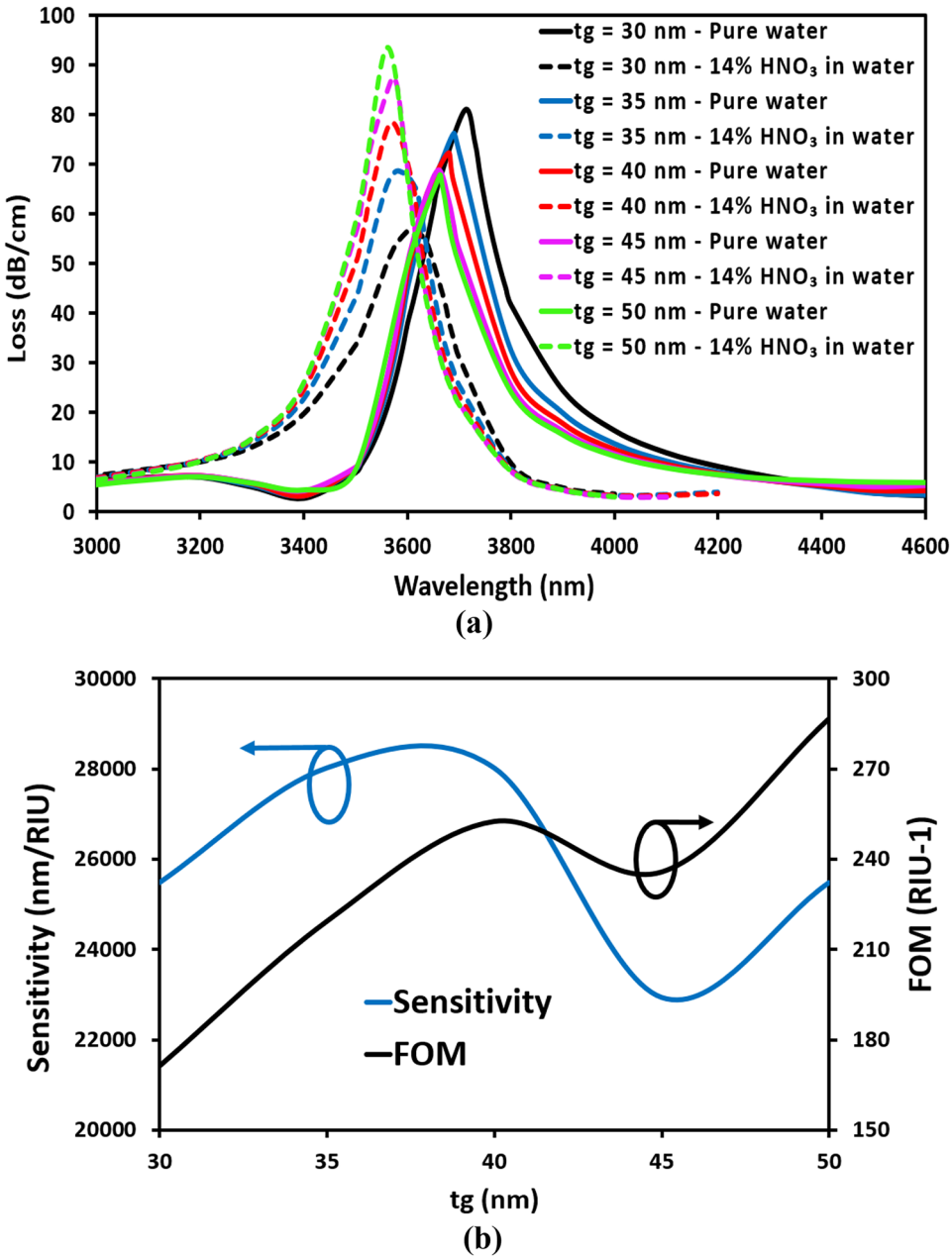

Fig. 7 **a** Wavelength-dependent optical loss curves of the fundamental core mode at different values of t_g, and **b** the sensitivity (S) and FOM at different values of t_g. The other dimensions were $w_g = 0.4$ µm, $\eta = 0.7$, and $h = 5$ µm, respectively (as in Fig. 1b)

0.1, at constant $t_g = 50$ nm (see "Au Nano-grating Thickness (tg)" section) and constant $w_g = 0.4$ µm, $h = 5$ µm (as in Fig. 1b). From Fig. 8a, on increasing η from 0.6 to 0.8, the optical loss curves of the core fundamental mode for both pure and HNO_3 14% $^{v}/_{v}$ polluted water shift toward longer wavelengths. Thus, the resonance wavelengths (λ_r) are red shifted from 3380 to 4400 nm for pure water, and from 3360 to 4180 nm for polluted water. In comparing λ_r of pure water with that of water polluted with 14% $^{v}/_{v}$ HNO_3, λ_r is shifted to a shorter wavelength when water is polluted with 14% $^{v}/_{v}$ HNO_3 (Fig. 8a).

Figure 8b shows the sensitivity and FOM as a function of η. At $\eta = 0.8$, a high sensitivity of $S = 56{,}049$ nm/RIU is realized at (Fig. 8b) with high FOM of 743.3 RIU^{-1} due to a small FWHM of 75.4 nm. Although $\eta = 0.8$ gives the higher sensitivity and FOM, it has a low loss peak as shown from Fig. 8a. Accordingly, selecting $\eta = 0.8$ would reduce the amplitude sensitivity [52]. Instead, $\eta = 0.7$ is selected as the optimized value for high sensitivity, 25,476 nm/RIU and acceptable FOM, of 286.69 RIU^{-1}, with a high optical loss peak of 67.9 dB/cm and 93.48 dB/cm for pure and polluted water analytes, respectively. Additionally,

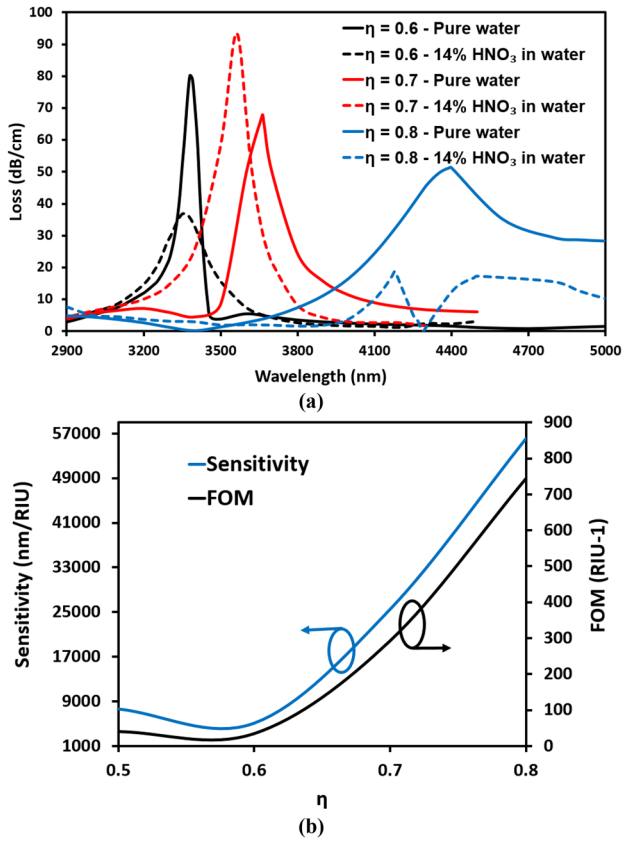

Fig. 8 **a** Wavelength dependent optical loss of core mode at different values of η, and **b** the sensitivity (S) and FOM at different values of η. The initial dimensions of $w_g = 0.4$ µm and $h = 5$ µm were used (see Fig. 1b). t_g was fixed at its optimized value of 50 nm

FWHM still has a small value of 88.9 nm and FOM reaches 286.7 RIU^{-1}.

Au Nano-grating Width (w_g)

To investigate the influence of the Au nano-grating width (w_g) on sensor performance, w_g is varied from 0.4 to 1.6 µm while t_g, η, and h are fixed to 50 nm, 0.7, and 5 µm, respectively. Figure 9 shows the field distribution of the fundamental x-polarized core mode at different values of w_g. By increasing w_g from 0.4 to 1.2 µm, the field is pulled up (see Fig. 1b) from the InF_3-based glass fiber core region to the metal/dielectric (Au/InF_3-based glass) interface. In the simulation, this in turn enhances the SPM until a maximum coupling between the fundamental fiber core mode light and the SPM occurred at 1.2 µm (Fig. 9a–c). However, further increase in w_g decreases the coupling strength between the core mode and the SPM (Fig. 9d). So, the optical loss of the core mode is found to increase gradually as w_g is increased from 0.4 to 1.6 µm, reaching a sharp maximum peak at $w_g = 1.2$ µm (Fig. 10a). By increasing w_g beyond 1.2 µm, the core mode optical loss peak then reduces and broadens, i.e., FWHM increases. Moreover, increasing w_g induces a slight blue shift in the resonance wavelength, λ_r.

The numerical calculations that describe Fig. 9 can be shown in Fig. 10a. Figure 10a depicts the wavelength dependent optical loss spectra of the fundamental x-polarized core mode when w_g is varied from 0.4 to 1.6 µm, in 0.4 µm steps. By increasing w_g, λ_r is shifted to shorter wavelengths for both pure water and water polluted with 14% v/v HNO_3. It is worth

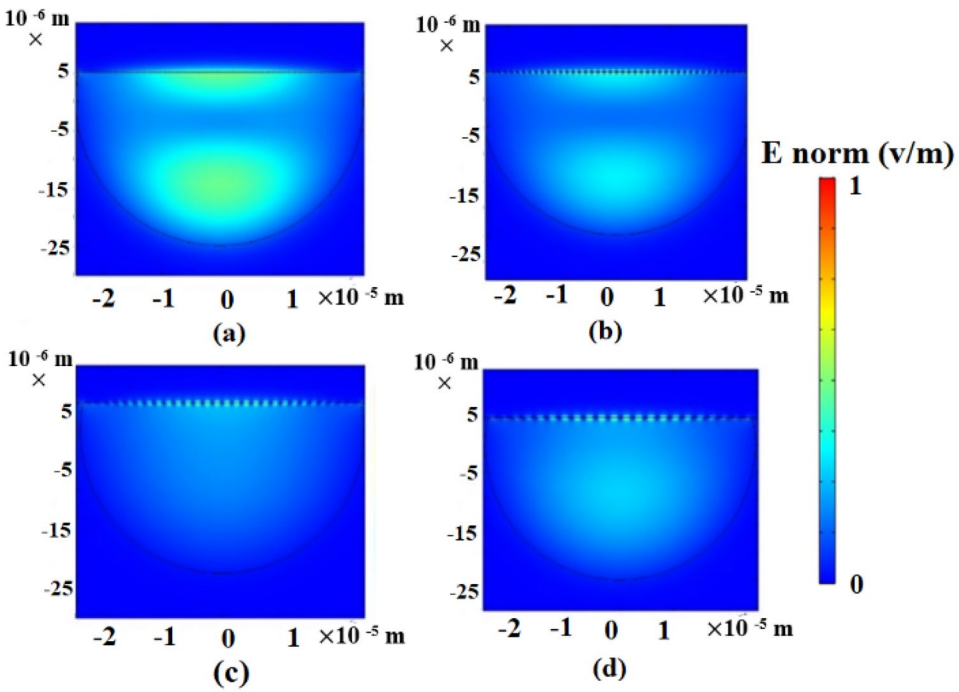

Fig. 9 E-field distributions at different values of wg: **a** 0.4 µm; **b** 0.8 µm; **c** 1.2 µm, and **d** 1.6 µm

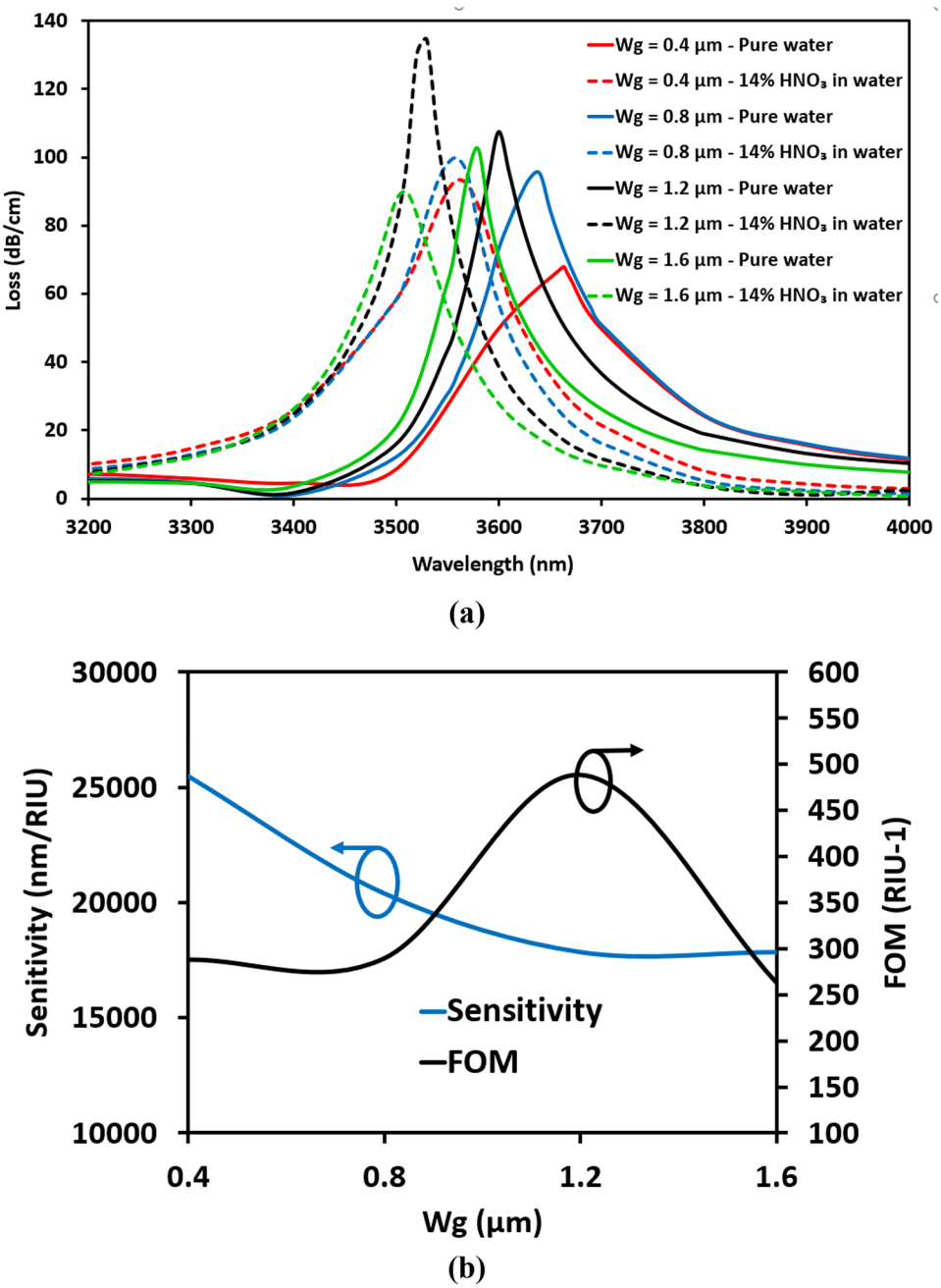

Fig. 10 **a** Wavelength dependent optical loss of the core mode at different values of w_g, and **b** the sensitivity (S, Eq. (3)) and FOM (Eq. (5)) at different values of w_g. The utilized initial dimension of h = 5 µm (as in Fig. 1b). t_g and η were fixed at their optimized values of 50 nm and 0.7, respectively

mentioning that by increasing w_g, the optical losses increase for both pure water and polluted water with 14% v/v HNO_3 until it reaches its maximum peak at $w_g = 1.2$ µm at resonance wavelength $\lambda_r = 3600$ nm (pure water) and 3530 nm (polluted water with 14% v/v HNO_3). Then, increasing w_g beyond 1.2 µm leads to a reduction in the optical losses for both pure water and polluted water with 14% v/v HNO_3. Figure 10b depicts the S (λ) and FOM of the proposed optical sensor as functions of w_g. It is revealed from this figure that a high sensitivity of 25,477 nm/RIU is obtained at $w_g = 0.4$ µm. However, $w_g = 0.4$ µm corresponds to a relatively large FWHM of ~ 88 nm with a low FOM of 288.5 RIU^{-1}.

Accordingly, choosing $w_g = 0.4$ µm would reduce the sensing accuracy of the D-shaped InF_3-based glass fiber sensor to detect the HNO_3 pollutant in water. Therefore, $w_g = 1.2$ µm is selected as being optimal overall as the sharpest loss peak occurs here with the minimum FWHM of 36.5 nm; see Fig. 10a. Further, a maximum FOM of 488.8 RIU^{-1} and high sensitivity of 17,834 nm/RIU are also achieved at $w_g = 1.2$ µm, as shown in Fig. 10b.

Distance from Side-Polished Surface of Fiber to Center of Fiber Core (h)

The effect on sensor performance of the distance from the side-polished surface to the fiber core center (h) is then investigated. It is worth noting that the fiber core diameter is 50 µm (see Fig. 1b) and h values of 3 µm, 4 µm, 5 µm, 6 µm, and 7 µm are studied (Fig. 10) for fixed values of t_g, η, and w_g of 50 nm, 0.7, and 1.2 µm, respectively (see Sections "Au Nano-grating Thickness (tg)", "Au Nano-grating Duty Cycle (η)", and "Au Nano-grating Width (wg)", respectively). From Fig. 11a, increasing h causes the confinement optical loss of the fiber core mode to slightly decrease for both the pure water and polluted water. In addition, for h increases from 3 to 4 µm, λ_r of pure water is slightly shifted from 3610 down to 3600 nm (Fig. 11a). It is worth noting that h has a limited influence on λ_r as depicted in Fig. 11a. Figure 11b shows that by increasing h from 3 to 4 µm, the sensitivity (S, Eq. (1)) decreases from 20,381 to 17,834 nm/RIU, while the sensitivity is nearly constant on further increasing h beyond 4 µm. However, at h = 3 µm, a high sensitivity is achieved with small FOM. Therefore, the optimized value of h is chosen to be 4 µm since it gives the highest FOM of 487 RIU^{-1} with a relatively high sensitivity of 17,834 nm/RIU.

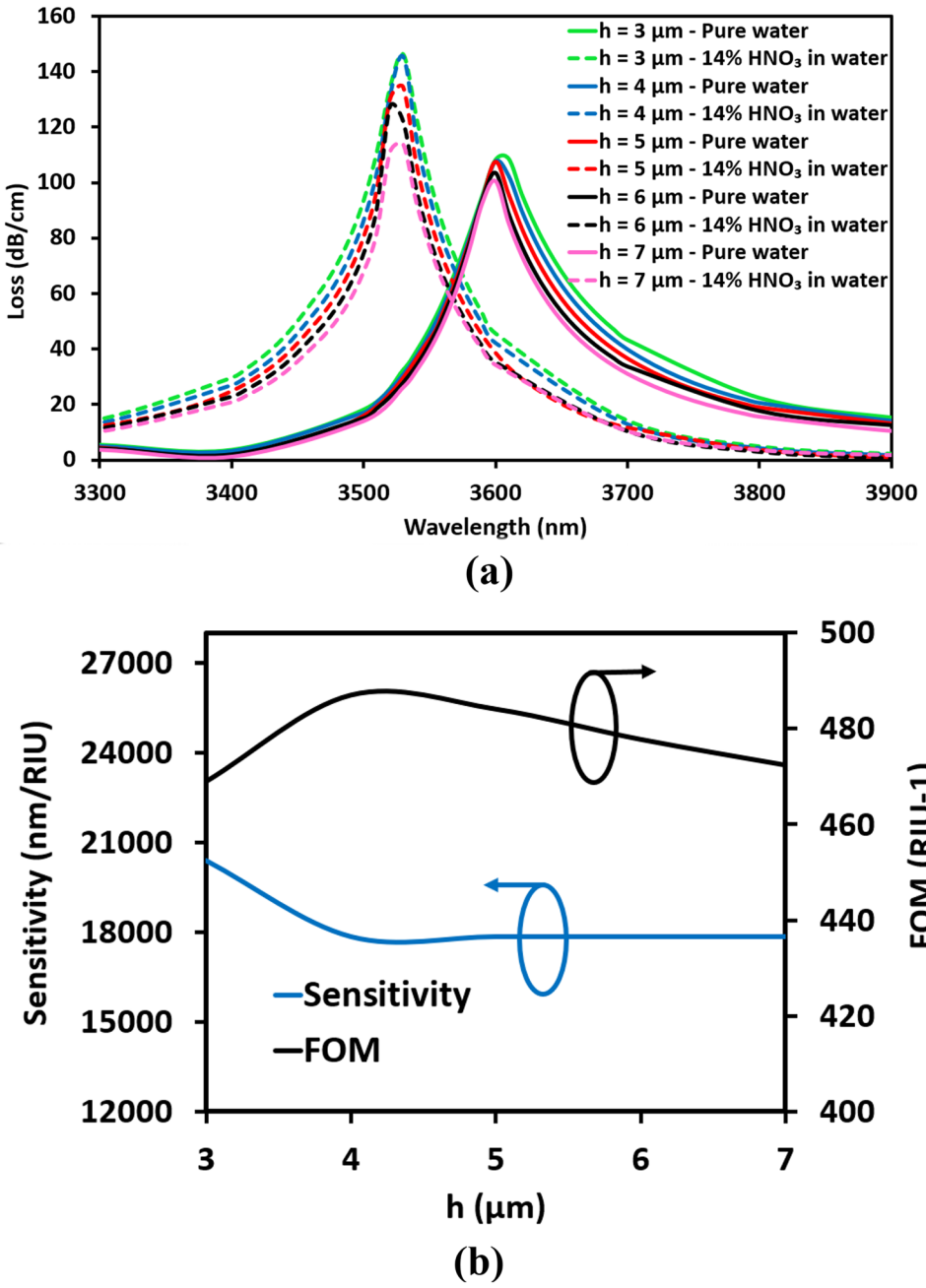

Fig. 11 **a** Wavelength dependent optical loss of the core mode at different values of h, and **b** the sensitivity and FOM for different values of h. All other dimensions were fixed to their optimized values as $t_g = 50$ nm, $\eta = 0.7$, $w_g = 1.2$ µm, and h = 4 µm (*cf.* Fig. 1b starting values of these parameters)

Table 1 The fabrication tolerance as expressed by sensor sensitivity (S (λ)) of the optimized D-shaped InF_3-based glass optical fiber, for detecting the 14% $^{v}/_{v}$ HNO_3 in water. Each geometric parameter is varied consecutively within ± 5% of the optimized value, while keeping the other geometric parameters static at the optimized value

Geometrical parameter	Optimum value	Sensitivity (S)/(nm/RIU)		
		Optimized *S*	*S* for optimized geometrical parameter + 5%	*S* for optimized geometrical parameter - 5%
t_g	50 nm	17,834	17,834	17,834
η	0.7	17,834	17,834	20,381
w_g	1.2 µm	17,834	20,381	20,381
h	4 µm	17,834	17,834	17,834

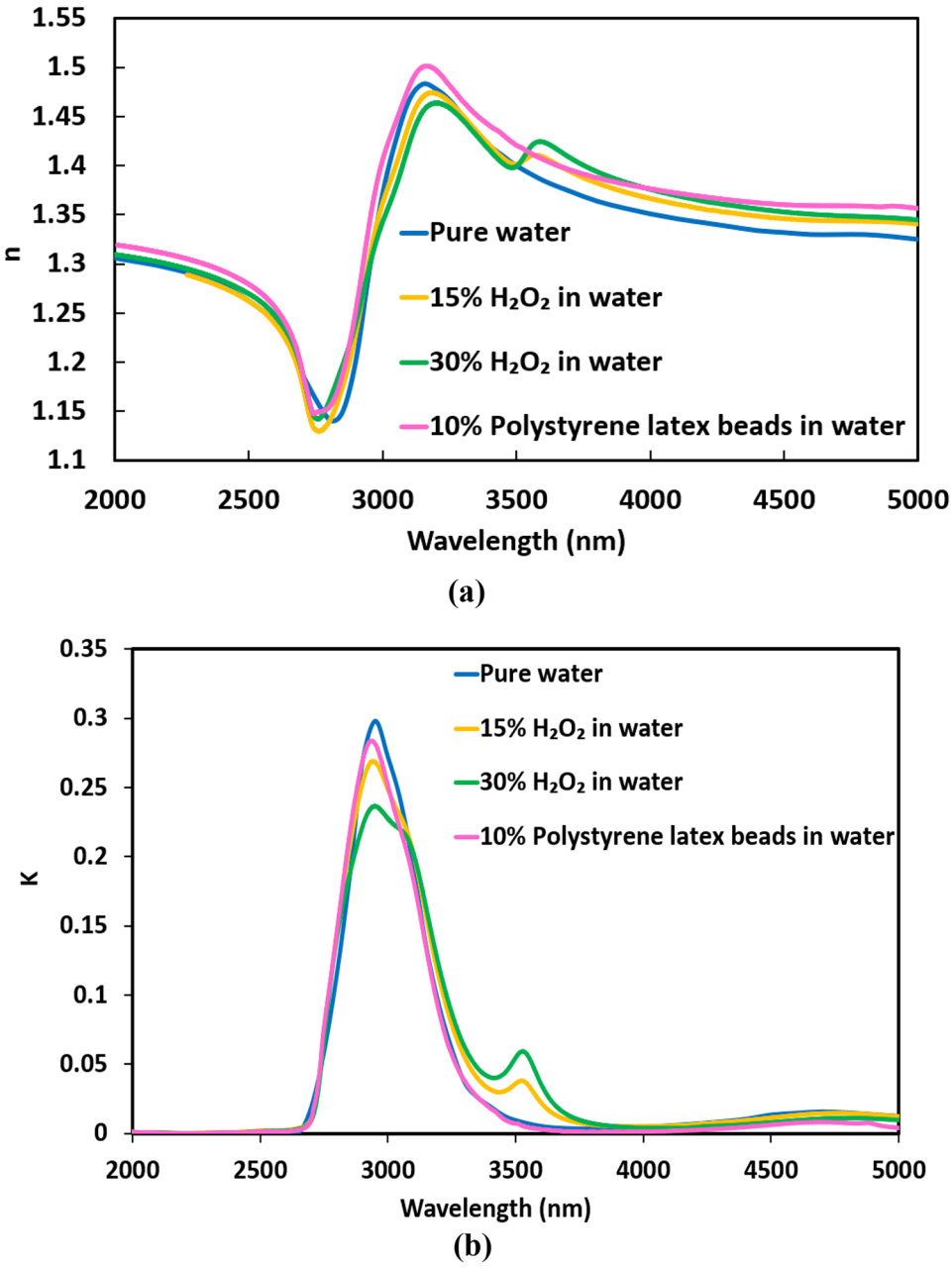

Fig. 12 **a** The real part and **b** imaginary part (extinction coefficient) of the refractive index of pure water and those of dissolved 15% $^{v}/_{v}$ H_2O_2 in water, 30% $^{v}/_{v}$ H_2O_2, and suspended 10%$^{v}/_{v}$ polystyrene 0.1 µm diameter beads in water [44, 45]

Summary of Optimized Au Nano-grating Parameters of the Sensor

The optimal structural parameters of the proposed D-shaped InF_3-based glass optical fiber sensor are listed in Table 1 at which a high sensitivity of 17,834 nm/RIU and high FOM of 487 RIU^{-1} are attained. Note that the sensor is specifically optimized for a pollutant of 14% $^{v}/_{v}$ HNO_3 in water.

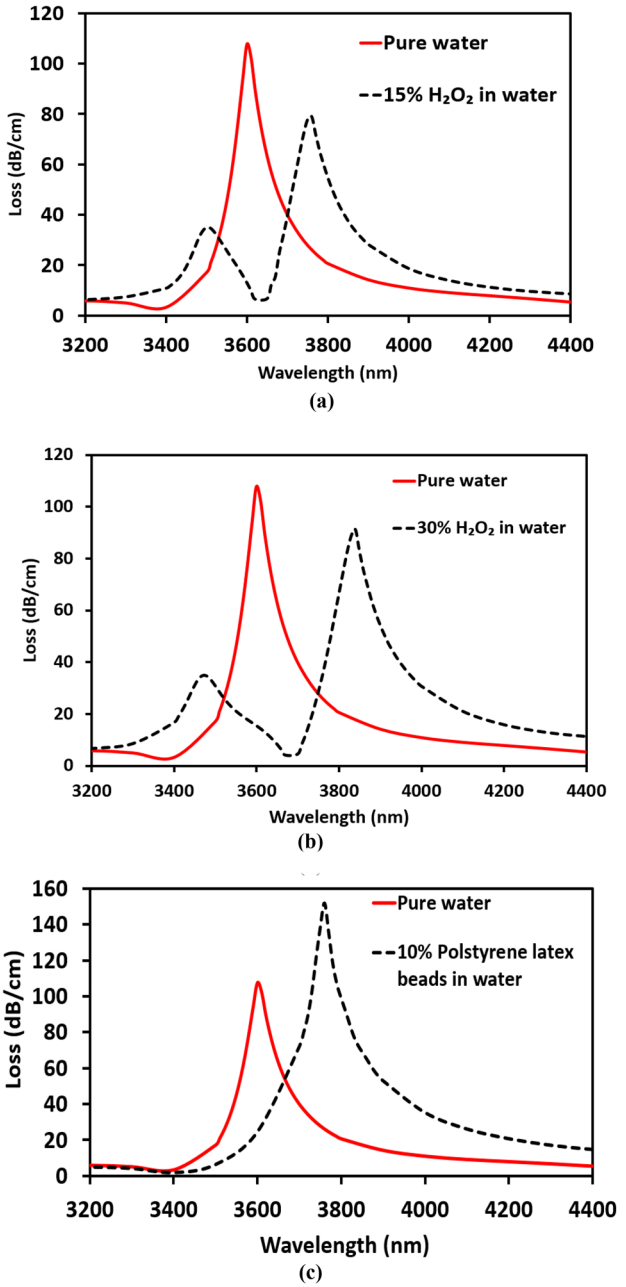

Fig. 13 Confinement optical loss spectra of the core mode of the geometrically optimized (Table 1) D-shaped InF_3-based glass optical fiber SPR sensor for pure water and **a** dissolved 15% $^{v}/_{v}$ H_2O_2 in water, **b** dissolved 30% $^{v}/_{v}$ H_2O_2 in water, **c** suspended10% $^{v}/_{v}$ polystyrene 0.1 µm diameter beads in water

Projected Fabrication Tolerance of Proposed Optimized Sensor

The fabrication tolerance of the proposed D-shaped SPR sensor design is investigated to look at its robustness to fabrication imperfections. Here, only one parameter is varied by ± 5% of its optimum value while the other geometrical parameters are kept at their optimum values as listed in Table 1. From the results in Table 1, it may be seen that the proposed water pollutant sensor exhibited sensitivity (S) better than 17,834 nm/RIU for all geometric parameters, which ensures stable performance when each parameter is varied between ± 5% of its optimized value.

Sensor Detection of Other Pollutants in Water

Using the proposed D-shaped InF_3-based glass optical fiber SPR sensor to detect water pollutants other than HNO_3 is explored, viz. hydrogen peroxide (H_2O_2), miscible with water, in $^{v}/_{v}$ concentrations of 15% and 30%, and polystyrene beads, immiscible with water, in $^{v}/_{v}$ concentration of 10%. The real and imaginary parts of the refractive indices of these pollutants in the MIR range are taken from [47] and are plotted with the pure water RI in Fig. 12a, b, respectively. As shown in Fig. 12a, the RIs curves of pure water and polluted water (with 15% $^{v}/_{v}$ H_2O_2, 30% $^{v}/_{v}$ H_2O_2, and 10% $^{v}/_{v}$ polystyrene beads in water) have a dip around $\lambda = 2770$ nm. Additionally, around $\lambda = 3150$ nm, the RIs of pure water and polluted water (with 15% $^{v}/_{v}$ H_2O_2, 30% $^{v}/_{v}$ H_2O_2, and 10% $^{v}/_{v}$ polystyrene beads in water) reach its maximum value. Additionally, the maximum value of the extinction coefficient for pure water and polluted water (with 15% $^{v}/_{v}$ H_2O_2, 30% $^{v}/_{v}$ H_2O_2, and 10% $^{v}/_{v}$ polystyrene beads in water) occurs around $\lambda = 2950$ nm (Fig. 12b). It is worth noting that H_2O_2 is used for water disinfection purposes [53]. However, increasing the concentration of H_2O_2 beyond 5% in water causes skin irritation and possible burns, while eye contact may result in permanent eye damage. Also, it may cause severe digestive and respiratory tract irritation [54, 55]. Therefore, detection of 15% $^{v}/_{v}$ H_2O_2 and 30% $^{v}/_{v}$ H_2O_2 in water is investigated here. By adding the solublecontaminant, 15% $^{v}/_{v}$ H_2O_2 and 30% $^{v}/_{v}$ H_2O_2, to pure water, both the real and imaginary parts of the water refractive index change (Fig. 12a, b). Therefore, a shift in λ_r of the confinement loss peak which corresponds to the core mode is expected to occur by replacing the pure water sample with a polluted one.

The sensitivity of the optimized sensor (see Table 1) towards various pollutants in water, viz. H_2O_2 (15% $^{v}/_{v}$ and 30% $^{v}/_{v}$) and polystyrene 0.1 µm diameter beads (10% $^{v}/_{v}$). Figure 13a–c shows the wavelength-dependent confinement loss of the fundamental core mode in the D-shaped InF_3-based glass optical fiber sensor of pure water and water with 15% $^{v}/_{v}$ H_2O_2, 30% $^{v}/_{v}$ H_2O_2, and 10% $^{v}/_{v}$ polystyrene beads, respectively.

Table 2 Performance analysis of the SPR sensor with different pollutants: H_2O_2 and polystyrene 0.1 µm diameter beads

Pollutant	$\Delta\lambda_r$ / (nm)	*S* / (nm/RIU)	FWHM / (nm)	FOM / (RIU^{-1})
14% $^{v}/_{v}$ HNO_3	70	17834	36.5	487
15% $^{v}/_{v}$ H_2O_2	160	12308	77	160
30% $^{v}/_{v}$ H_2O_2	240	17143	82	209
10% $^{v}/_{v}$ polystyrene beads	160	5333	56	96

Table 3 Comparison of the sensing performance of the proposed device and those reported in the literature

Device	Sensing Platform		S / (nm/RIU)	FOM / (RIU^{-1})	RI range	Wavelength range
Ref. [23]	D-shaped *silica glass* fiber		6400	56.5	1.33–1.39	Visible
Ref. [25]			1566	1021.2	1.3–1.335	NIR
Ref. [26]			4471	-	1.33–1.38	NIR
Ref. [27]			15310	91	1.325–1.355	NIR
Ref. [56]			925	-	1.35–1.43	NIR
Ref. [37]			2260	25	1.333–1.390	NIR
Ref. [38]	D-shaped *plastic* fiber		4793	-	1.335–1.410	NIR
Ref. [40]	Dual-tapered *silica glass* fiber tip		4470	-	1–1.7	MIR (9–18 µm)
This work	D-shaped *InF_3-based glass fiber*	14% $^{v}/_{v}$ HNO_3	17834	487	1.362–1.366	MIR (3–4.5 µm)
		15% $^{v}/_{v}$ H_2O_2	12308	160	1.362–1.375	
		30% $^{v}/_{v}$ H_2O_2	17143	209	1.362–1.376	
		10% $^{v}/_{v}$ polystyrene	5333	96	1.362–0.392	

From Fig. 13a for 15% $^{v}/_{v}$ *aq.* H_2O_2, the resonance wavelength shifts from 3600 nm (in the case of pure water) to 3760 nm (corresponding to the maximum peak in the case of 15% $^{v}/_{v}$ *aq.* H_2O_2). Thus, a $\Delta\lambda_r$ of 160 nm is obtained, leading to a sensitivity of 12,308 nm/RIU and FOM of 160 RIU^{-1} as summarized in Table 2. As the concentration of H_2O_2 in water is further increased to 30% $^{v}/_{v}$, λ_r increases to 3840 nm (Fig. 13b). In this case, the calculated sensitivity and FOM are equal to 17,143 nm/RIU and 209 RIU^{-1}, respectively. However, adding polystyrene 0.1 µm diameter beads to water with a concentration of 10% $^{v}/_{v}$ induced a λ_r of 3760 nm (Fig. 13c). Hence, the sensitivity in this case is calculated to be 5333 nm/RIU while the FOM is 96 RIU^{-1}.

Table 3 depicts a comparison summary of the performance of the InF_3-based glass optical fiber device proposed in this paper with that of previously reported optical fiber-based SPR sensors all of which were based on silica glass optical fibers; the comparison is made in terms of the sensor type, sensitivity, FOM, RI range, and operating wavelength range. The proposed design exhibits the highest sensitivity with comparable FOM when compared with those reported in [23, 25–27, 37, 38, 40, 56].

Conclusion

A MIR (mid-infrared) optical fiber sensor for water pollution detection is proposed and numerically analyzed for the first time to the Authors' knowledge. The proposed sensor is based on a D-shaped InF_3-based glass optical fiber with a gold grating structure deposited on the polished surface and depends on the SPR sensing mechanism. The geometrical dimensions of the Au grating are optimized. The proposed sensor can detect different pollutants in water such as 14% $^{v}/_{v}$ (percent by volume) HNO_3, 15% $^{v}/_{v}$ and 30% $^{v}/_{v}$ H_2O_2, and 10% $^{v}/_{v}$ polystyrene 0.1 µm diameter beads. The sensing characteristics of the proposed sensor are analyzed using FVFEM (full vectorial finite element method) in the MIR fundamental vibrational absorption wavelength regime from 2900 to 4500 nm. In addition, the reported D-shaped optical fiber sensor is proven robust to fabrication errors in geometrical parameters by ± 5%. The obtained results reveal that a high sensitivity of 17,834 nm/RIU, 12,308 nm/RIU, 17,143 nm/RIU, and 5,333 nm/RIU was achieved for the detection of 14% $^{v}/_{v}$ HNO_3, 15% $^{v}/_{v}$ H_2O_2, 30% $^{v}/_{v}$ H_2O_2, and 10% $^{v}/_{v}$ polystyrene beads in water sensing mechanism, respectively.

The geometrical dimensions of the Au grating are optimized. The proposed sensor has a FOM of 487 RIU^{-1}, 160 RIU^{-1}, 209 RIU^{-1}, and 96 RIU^{-1} for 14% $^{v}/_{v}$ HNO_3, 15% $^{v}/_{v}$ H_2O_2, 30% $^{v}/_{v}$ H_2O_2, and 10% $^{v}/_{v}$ polystyrene beads in water, respectively. Therefore, the reported sensor has the advantages of a simple design, yet higher sensitivity than similar sensors reported in the literature with a comparable FOM. The key to the higher sensor sensitivity found here is in applying SPM in the MIR wavelength regime using a MIR-transparent InF_3-based glass optical fiber, D-shaped, as opposed to the work of others where SPM was applied in the visible or near-infrared regime using silica-glass fiber optics.

Author Contribution B. M. Younis, Nada Yazeed M. Dawood, Ahmed El-Sayed Abd-Elkader, and Mohamed Farhat O. Hameed, have proposed the idea. Nada Yazeed M. Dawood and B. M. Younis have done the simulations of the reported sensor. All authors have contributed to the analysis, discussion, writing, and revision of the paper.

Funding Open access funding provided by The Science, Technology & Innovation Funding Authority (STDF) in cooperation with The Egyptian Knowledge Bank (EKB). The authors acknowledge the financial support received from the Science, Technology & Innovation Funding Authority (STIFA), Egypt, under Newton-Mosharafa Impact Scheme (ID:43934).

Data Availability The data will be available upon request.

Declarations

Competing Interests The authors declare no competing interests.

References

1. Madhav S, Ahamad A, Singh AK, Kushawaha J, Chauhan JS, Sharma S, Singh P (2020) Water pollutants: sources and impact on the environment and human health. Sensors in water pollutants monitoring: role of material. pp 43–62
2. Bringmann G, Kühn R (1980) Comparison of the toxicity thresholds of water pollutants to bacteria, algae, and protozoa in the cell multiplication inhibition test. Water Res 14:231–241
3. Duruibe JO, Ogwuegbu MOC, Egwurugwu JN (2007) Heavy metal pollution and human biotoxic effects. Int J Phys Sci 2:112–118
4. Zahir F, Rizwi SJ, Haq SK, Khan RH (2005) Low dose mercury toxicity and human health. Environ Toxicol Pharmacol 20:351–360
5. Dong Z, Wang L, Xu J, Li Y, Zhang Y, Zhang S, Miao J (2009) Promotion of autophagy and inhibition of apoptosis by low concentrations of cadmium in vascular endothelial cells. Toxicol In Vitro 23:105–110
6. Rattner BA (2009) History of wildlife toxicology. Ecotoxicology 18:773–783
7. Hooda PS, Edwards AC, Anderson HA, Miller A (2000) A review of water quality concerns in livestock farming areas. Sci Total Environ 250:143–167
8. ashir I, Lone FA, Bhat RA, Mir SA, Dar ZA, Dar SA (2020) Concerns and threats of contamination on aquatic ecosystems. Bioremediation and biotechnology: sustainable approaches to pollution degradation. pp 1–26
9. Islam MS, Tanaka M (2004) Impacts of pollution on coastal and marine ecosystems including coastal and marine fisheries and approach for management: a review and synthesis. Mar Pollut Bull 48:624–649
10. Hameed MFO, Obayya S (2019) Computational photonic sensors. Springer
11. Pejcic B, Eadington P, Ross A (2007) Environmental monitoring of hydrocarbons: a chemical sensor perspective. Environ Sci Technol 41:6333–6342
12. Sieger M, Haas J, Jetter M, Michler P, Godejohann M, Mizaikoff B (2016) Mid-infrared spectroscopy platform based on GaAs/AlGaAs thin-film waveguides and quantum cascade lasers. Anal Chem 88:2558–2562
13. Kim SS, Young C, Mizaikoff B (2008) Miniaturized mid-infrared sensor technologies. Anal Bioanal Chem 390:231–237
14. Azzam SI, Hameed MFO, Shehata REA, Heikal AM, Obayya SSA (2016) Multichannel photonic crystal fiber surface plasmon resonance-based sensor. Opt Quant Electron 48:1–11
15. Piliarik M, Homola J, Manıková Z, Čtyroký J (2003) Surface plasmon resonance sensor based on a single-mode polarization-maintaining optical fiber. Sens Actuators B Chem 90:236–242
16. Tamersit K, Djeffal F (2016) Double-gate graphene nanoribbon field-effect transistor for DNA and gas sensing applications: simulation study and sensitivity analysis. IEEE Sens J 16:4180–4191
17. Ouyang Q, Zeng S, Jiang L, Hong L, Xu G, Dinh XQ, Qian J, He S, Qu J, Coquet P (2016) Sensitivity enhancement of transition metal dichalcogenides/silicon nanostructure-based surface plasmon resonance biosensor. Sci Rep 6:1–13
18. Erdmanis M, Viegas D, Hautakorpi M, Novotny S, Santos JL, Ludvigsen H (2011) Comprehensive numerical analysis of a surface-plasmon-resonance sensor based on an H-shaped optical fiber. Opt Express 19:13980–13988
19. Min R, Liu Z, Pereira L, Yang C, Sui Q, Marques C (2021) Optical fiber sensing for marine environment and marine structural health monitoring: a review. Opt Laser Technol 140:107082
20. Sharma AK, Jha R, Gupta BD (2007) Fiber-optic sensors based on surface plasmon resonance: a comprehensive review. IEEE Sens J 7:1118–1129
21. Wang S, Li S (2019) Surface plasmon resonance sensor based on symmetrical side-polished dual-core photonic crystal fiber. Opt Fiber Technol 51:96–100
22. Caucheteur C, Guo T, Albert J (2015) Review of plasmonic fiber optic biochemical sensors: improving the limit of detection. Anal Bioanal Chem 407:3883–3897
23. Kadhim RA, Yuan L, Xu H, Wu J, Wang Z (2020) Highly sensitive D-shaped optical fiber surface plasmon resonance refractive index sensor based on Ag-α-Fe_2O_3 grating. IEEE Sens J 20:9816–9824
24. Verma R, Gupta BD (2015) Detection of heavy metal ions in contaminated water by surface plasmon resonance based optical

fiber sensor using conducting polymer and chitosan. Food Chem 166:568–575
25. Del Villar I, Zubiate P, Zamarreño CR et al (2017) Optimization in nanocoated D-shaped optical fiber sensors. Opt Express 25:10743–10756
26. Pathak AK, Rahman BMA, Singh VK, Kumari S (2019) Sensitivity enhancement of a concave shaped optical fiber refractive index sensor covered with multiple Au nanowires. Sensors 19:4210
27. Dubey SK, Kumar A, Kumar A, A. Pathak A, Srivastava SK, (2022) A study of highly sensitive D-shaped optical fiber surface plasmon resonance based refractive index sensor using grating structures of Ag-TiO2 and Ag-SnO2. Optik 252:168527
28. Mizaikoff B (2003) Infrared optical sensors for water quality monitoring. Water Sci Technol 47:35–42
29. ISO BSI (2015) 20473: 2007 Optics and Photonics—Spectral Bands
30. Snopatin GE, Shiryaev VS, Plotnichenko VG, Dianov EM, Churbanov MF (2009) High-purity chalcogenide glasses for fiber optics. Inorg Mater 45:1439–1460
31. Almeida RM (2012) Halide glasses for infrared fiberoptics. Springer Science & Business Media
32. Saad M (2012) Indium fluoride glass fibers. In: Laser Refrigeration of Solids V. SPIE. pp 64–69
33. Goya K, Koyama Y, Nishijima Y, Tokita S, Yasuhara R, Uehara H (2022) A fluoride fiber optics in-line sensor for mid-IR spectroscopy based on a side-polished structure. Sens Actuators B Chem 351:130904
34. Obayya SSA, Rahman BMA, El-Mikati HA (2000) New full-vectorial numerically efficient propagation algorithm based on the finite element method. J Lightwave Technol 18:409
35. Obayya SSA, Rahman BMA, El-Mikati HA (2000) Full-vectorial finite-element beam propagation method for nonlinear directional coupler devices. IEEE J Quantum Electron 36:556–562
36. Obayya SSA, Rahman BMA, Grattan KTV, El-Mikati HA (2002) Full vectorial finite-element solution of nonlinear bistable optical waveguides. IEEE J Quantum Electron 38:1120–1125
37. Liu L, Liu Z, Zhang Y, Liu S (2021) Side-polished D-type fiber SPR sensor for RI sensing with temperature compensation. IEEE Sens J 21:16621–16628
38. Kadhim RA, Abdul AK, Yuan L (2022) Advances in surface plasmon resonance-based plastic optical fiber sensors. IETE Tech Rev 39:442–459
39. Li X, Liang J, Li J, Ye J, Liu Y, Chen M, Zhang Z, Qu S (2022) Highly sensitive curvature, and temperature sensor based on double groove structure and hollow core fiber. IEEE Sens J 22:9454–9461
40. Zhou X, Yu Q, Peng W (2019) Mid-infrared surface plasmon resonance sensor based on silicon-doped InAs film and chalcogenide glass fiber. Opt Laser Technol 120:105686
41. Salem R, Jiang Z, Liu D, Pafchek R, Gardner D, Foy P, Saad M, Jenkins D, Cable A, Fendel P (2015) Mid-infrared supercontinuum generation spanning 1.8 octaves using step-index indium fluoride fiber pumped by a femtosecond fiber laser near 2 µm. Opt Express 23:30592–30602
42. Wang C, Chen PJ, Hsueh CH (2022) Au-based thin-film metallic glasses for propagating surface plasmon resonance-based sensor applications. ACS Omega 7:18780–18785
43. Qu Y, Yuan J, Zhou X, Li F, Mei C, Yan B, Wu Q, Wang K, Sang X, Long K (2019) A V-shape photonic crystal fiber polarization filter based on surface plasmon resonance effect. Optics Communications 452:1–6
44. COMSOL 5.1, https://www.comsol.com
45. Koshiba M, Tsuji Y (2000) Curvilinear hybrid edge/nodal elements with triangular shape for guided-wave problems. J Light Technol 18:737–743
46. Dawood NYM, Younis BM, Areed NFF, Hameed MFO, Obayya SSA (2021) Mid-infrared optical modulator based on silicon D-shaped photonic crystal fiber with VO 2 material. Appl Opt 60:9488–9496
47. Myers TL, Tonkyn RG, Danby TO, Taubman MS, Bernacki BE, Birnbaum JC, Sharpe SW, Johnson TJ (2018) Accurate measurement of the optical constants n and k for a series of 57 inorganic and organic liquids for optical modeling and detection. Appl Spectrosc 72:535–550
48. Hale GM, Querry MR (1973) Optical constants of water in the 200-nm to 200-µm wavelength region. Appl Opt 12:555–563
49. Rifat AA, Mahdiraji GA, Chow DM, Shee YG, Ahmed AFRM (2015) Photonic crystal fiber-based surface plasmon resonance sensor with selective analyte channels and graphene-silver deposited core. Sensors 15:11499–11510
50. Saber AM, Hameed MFO, El-Azab J, Amer RY, Ismail T, Obayya SSA (2022) Plasmonic photonic crystal fiber sensor for optical partial discharge detection. Opt Quant Electron 54:433
51. Qin W, Li SG, Xue JR, Xin XJ, Zhang L (2013) Numerical analysis of a photonic crystal fiber based on two polarized modes for biosensing applications. Chin Phys B 22:74213
52. Fang H, Wei C, Yang H, Zhao B, Yuan L, Li J (2021) D-shaped photonic crystal fiber plasmonic sensor based on silver-titanium dioxide composite micro-grating. Plasmonics 16:2049–2059
53. Arends JBA, Van Denhouwe S, Verstraete W, Boon N, Rabaey K (2014) Enhanced disinfection of wastewater by combining wetland treatment with bioelectrochemical H2O2 production. Bioresour Technol 155:352–358
54. H2O2, https://www.lenntech.com/processes/disinfection/chemical/disinfectants-hydrogen-peroxide.htm#:~:text=Hydrogen%20peroxide%20solutions%20look%20like,%20low%20temperatures%20it%20becomes%20solid
55. 30% H2O2, http://www.soest.hawaii.edu/krubin/MSDS/H2O2.html
56. Ying Y, Wang J, Hu N, Xu K, Sun L, Si G (2020) Determination of refractive index using surface plasmon resonance (SPR) and rigorous coupled wave analysis (RCWA) with a D-shaped optical fiber and a nano-gold grating. Instrum Sci Technol 48:376–385